

JGR Space Physics

RESEARCH ARTICLE

10.1029/2021JA029169

Key Points:

- Resonant ionospheric signatures observed after Sumatra 2012 doublet earthquake could be linked to seismic sources
- Resonant ionospheric signatures can provide more insight into rupture process of large earthquakes
- Effects of geomagnetic field coupling factor and satellite geometry on co-seismic ionospheric signals can be inconclusive

Supporting Information:

Supporting Information may be found in the online version of this article.

Correspondence to:



M. S. Bagiya,
bagiyamala@gmail.com;
mala.bagiya@igm.res.in

Citation:

Nayak, S., Bagiya, M. S., Maurya, S., Hazarika, N. K., Kumar, A. S. S., Prasad, D. S. V. V. D., & Ramesh, D. S. (2021). Terrestrial resonant oscillations during the 11 April 2012 Sumatra doublet earthquake. *Journal of Geophysical Research: Space Physics*, 126, e2021JA029169. <https://doi.org/10.1029/2021JA029169>

Received 25 JAN 2021
 Accepted 12 NOV 2021

Terrestrial Resonant Oscillations During the 11 April 2012 Sumatra Doublet Earthquake

Srinivas Nayak¹ , Mala S. Bagiya¹ , Satish Maurya², Nava Kumar Hazarika¹, A. S. Sunil Kumar³, D. S. V. V. D. Prasad⁴, and D. S. Ramesh⁵

¹Shillong Geophysical Research Center, Indian Institute of Geomagnetism, Shillong, India, ²Department of Earth Sciences, Indian Institute of Technology, Bombay, India, ³Anakuzhikkal House, Kannur, India, ⁴Department of Physics, Andhra University, Visakhapatnam, India, ⁵Indian Institute of Geomagnetism, Navi Mumbai, India

Abstract The Earth's background free oscillations at ~ 3.7 and ~ 4.4 mHz resonantly couple with the atmospheric acoustic modes and thus energy cross-talk between the earth-atmosphere system is maximum at these frequencies. The present study proposes resonant coupling between the Earth's surface and atmosphere during the 11 April 2012 Sumatra doublet earthquake and offer a possible explanation to this occurrence. Following both these earthquakes, prolonged ionospheric oscillations centered at frequency of ~ 4 mHz were observed in GPS (Global Positioning System) derived total electron content (TEC) towards north-northeast of the epicenters. We scrutinize these oscillations in terms of the manifestations of plausible non-tectonic and tectonic forcing mechanisms surrounding the epicentral region. Non-tectonic forcing such as the geomagnetic field coupling factor and observation geometry played a critical role in determining the amplitude anisotropy of resonant ionospheric signatures. Further, the Rayleigh waves of the first earthquake (Mw 8.6) were already characterized by an excess of energy at ~ 4 mHz. We propose this could make the Mw 8.6 earthquake particularly efficient to excite the 4 mHz resonance in the atmosphere. The resonant ionospheric signatures after the second earthquake (Mw 8.2) were observed to be closely associated with the Earth's free oscillations caused by R2 Rayleigh wave train of the Mw 8.6 earthquake event. Together, all the above point to a scenario where the resonant ionospheric signatures during the Sumatra doublet event were indeed related to the seismic source. Therefore, resonant co-seismic ionospheric signatures could provide additional information on the low-frequency features of seismic ruptures.

1. Introduction

An oscillating body when placed in a frictionless medium continues to oscillate and these are termed free oscillations. On the contrary, when a body continues to oscillate under the influence of an external periodic force, then such oscillations are known as forced oscillations. When the external force drives a body to its natural frequency, the resultant oscillations attain maximum amplitudes and are named as resonant oscillations. The Earth's surface is well-known to exhibit free oscillations at various spheroidal modes (mainly excited by compressional and shear forces) and toroidal modes (mostly by shear force) (Gilbert & Macdon, 1960; Kovach & Anderson, 1967). The excitation of the Earth's free surface oscillations is linked to various phenomena that operate inside or above the Earth's surface (Lognonne et al., 1998). For instance, the global atmospheric pressure disturbances and oceanic infrasonic gravity waves, localized events like strong convective storms and typhoons (Chum et al., 2017; Jones & Georges, 1976), in addition to earthquakes and volcanic eruptions, are considered as potential sources to excite the Earth's free oscillations at fundamental spheroidal modes of ${}_0S_{29}$ (3.72 mHz, 270s) and ${}_0S_{37}$ (4.44 mHz, 230s) (Fukao et al., 2002; Kanamori & Mori, 1992; Kobayashi & Nishida, 1998; Nawa et al., 1998; Nishida et al., 2000; Suda et al., 1998; Tanimoto et al., 1998). It has been theoretically estimated that the earth-atmospheric resonant coupling at acoustic frequencies is the most important process for atmospheric excitation of the Earth's surface (Lognonne et al., 1998; Watada, 1995; Watada & Kanamori, 2010). The fundamental Rayleigh surface waves at ~ 3.72 mHz resonantly couple with the fundamental atmospheric acoustic mode. Meanwhile, the Rayleigh waves at ~ 4.44 mHz resonantly oscillate with the first atmospheric acoustic overtone (Kanamori & Mori, 1992; Lognonné et al., 2006). The energy cross-talk between the Earth and its atmosphere is therefore maximum close to these frequency windows (Lognonne et al., 1998).

The seismic sources with vertical crustal displacement, and propagating co-seismic waves such as P, S, SS, and Rayleigh surface waves are the potential candidates which produce transient perturbations in the overlying

atmosphere/ionosphere system (Artru et al., 2004; Astafyeva & Heki, 2009; Astafyeva et al., 2011; Bagiya et al., 2017, 2018; Calais & Bernard, 1995; Chum et al., 2012; Ducic et al., 2003; Garcia et al., 2005; Maruyama et al., 2012; Rolland et al., 2011a, 2013; Sunil et al., 2017). The earthquake-induced Rayleigh surface waves excite the infrasonic acoustic waves in the adjacent atmosphere that propagate upward with growing amplitudes in a region of decreasing atmospheric neutral density. These seismic induced neutral wave perturbations interact with the ambient electron density at ionospheric altitudes through ion-neutral collision. This mechanism produces electron density perturbations termed as co-seismic ionospheric perturbations (CIP) and can be prominently observed through various radio techniques such as HF Doppler sounding (Chum et al., 2012; Chum & Podolská, 2018), ionosondes (Maruyama & Shinagawa, 2014) and Global Positioning System (GPS) measured total electron content (TEC) (Liu et al., 2011; Rolland, Lognonné, & Munekane, 2011; Tsugawa et al., 2011). However, in the GPS measured TEC, the amplitude and phase of an evolving CIP are modulated by non-tectonic forcing mechanisms such as geomagnetic field-acoustic wave coupling and moving satellite geometry which are operative at ionospheric altitudes (Rolland et al., 2013).

In addition to the transient CIP, prolonged ionospheric perturbations have been reported after the occurrence of great earthquakes ($M_w > 8.0$). For example, the continuous ionospheric disturbances for an hour or more after the Sumatra 2004 (Choosakul et al., 2009), Bengkulu 2007 (Cahyadi & Heki, 2013), Tohoku 2011 (Rolland, Lognonné, Astafyeva, et al., 2011) and Sumatra 2012 doublet earthquake (Cahyadi & Heki, 2015), Balochistan 2013 (Astafyeva et al., 2014) and Illapel 2015 earthquakes (Reddy et al., 2016) are few illustrations in this regard. It was demonstrated that these prolonged ionospheric perturbations fall in the frequency range ~ 3.72 and ~ 4.44 mHz. All these studies relate the observations mainly to resonant acoustic coupling between the Earth and its atmosphere via atmospheric trapped acoustic modes. However, these studies do not provide any specific evidence of their proposed mechanism.

The well-studied M_w 8.6, 11 April 2012, Sumatra doublet earthquake was the largest strike-slip event recorded in the history and was followed by another strike-slip earthquake of M_w 8.2 that occurred within ~ 2 hr of the first event (Singh et al., 2017; Yue et al., 2012). The events occurred at the center of the Wharton Basin, a major basin bounded to the west by the 90°E ridge (NER) and from North to East by the oblique Sumatran subduction (Figure 1). The M_w 8.6 and M_w 8.2 events ruptured the bilateral strike-slip faults trending WNW–ESE and NNE–SSW directions, at a depth of 26.3 and 21.6 km respectively (Duputel et al., 2012).

We explore the April 2012 Sumatra doublet earthquake sequence in the context of observed prolonged ionospheric perturbations centered at the frequency of ~ 4 mHz. We explain these ionospheric signatures in terms of acoustic resonant coupling between the terrestrial surface and its atmosphere. We observed that for the satellite IPP closer to the epicenter during the event recorded higher amplitude in TEC oscillations, but the amplitude dependence on satellite IPP distance was anisotropic around the epicenter. We discuss the possible mechanisms liable for the observed amplitude anisotropy of these perturbations around the epicenter, as amplitudes were largest and longest to NNE of the epicenter. The non-tectonic forcing mechanisms of geomagnetic field acoustic wave coupling and observation geometry assisted in explaining the amplitude anisotropy of resonant ionospheric signatures around the epicenters. To comprehend the role of ground seismic source, we propose that the excess energy manifestations at long period Rayleigh surface waves (~ 4 mHz) (Duputel et al., 2012) could contribute to excite the resonant ionospheric signatures following the M_w 8.6 Sumatra 2012 earthquake. The Earth's free oscillations as triggered by the R2 Rayleigh surface wave train after the first event (M_w 8.6) and subsequent atmospheric resonance could induce the prolonged ionospheric perturbations after the second earthquake event (M_w 8.2). Thus, the resonant ionospheric signatures after the Sumatra 2012 earthquake could be possibly linked to the seismic energy manifestations after the M_w 8.6 event.

2. Data

We analyze GPS ionospheric observations utilizing TEC data from 16 stations surrounding the Sumatra region on 11 April 2012 (Figure 1). The GPS stations of umlh, lewk, bsim, ptlo, bthl and btet are part of the Sumatran GPS Array (SuGAR) network, while the remaining are International GNSS Service (IGS) stations. We analyze the seismic data from 5 broadband stations surrounding the rupture area and the eastern part of the Indian Ocean (Figure 1). The seismic data were retrieved from the Incorporated Research Institutions for Seismology-Data Management Center (IRIS-DMC) (Trabant et al., 2012).

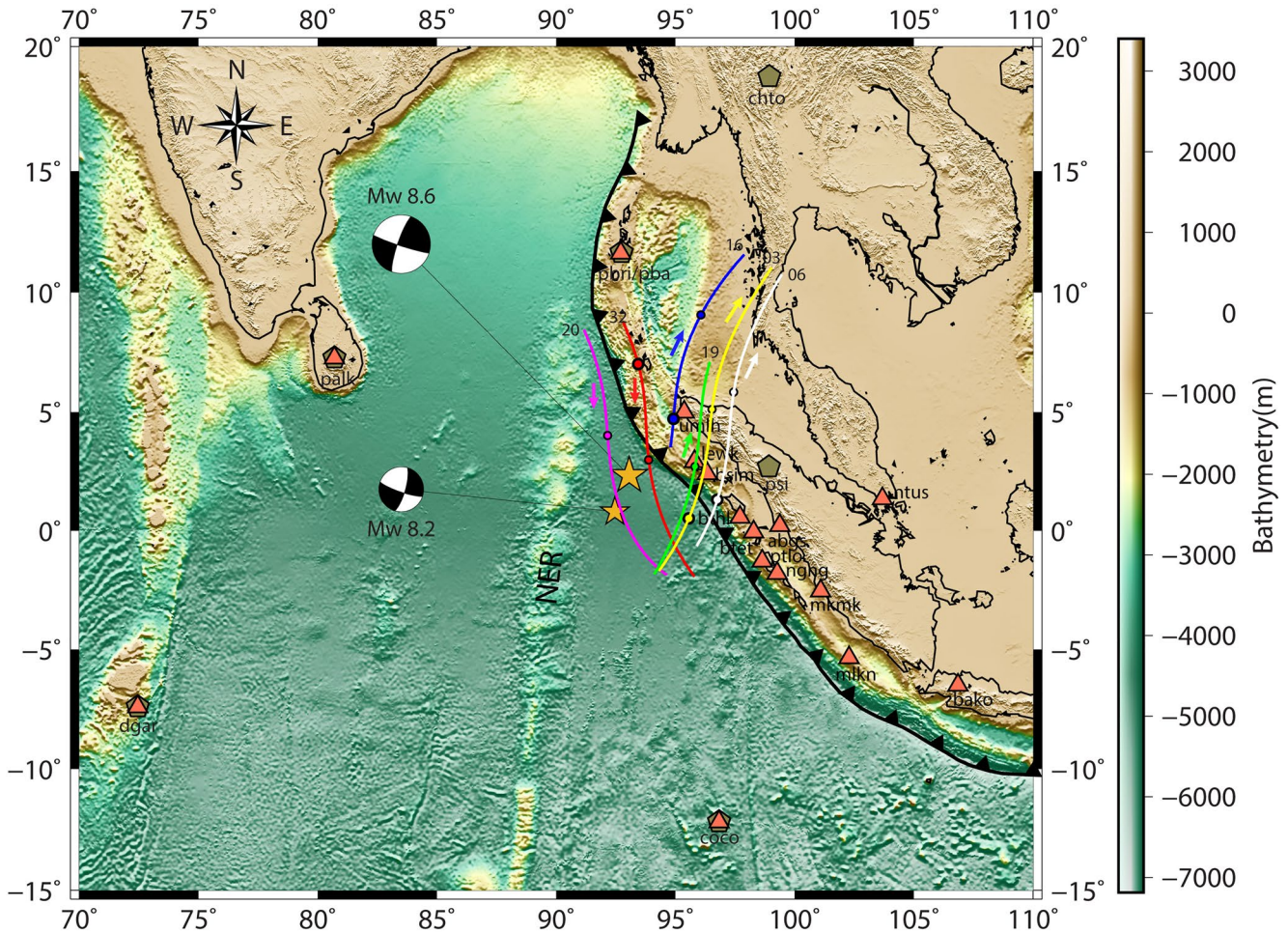


Figure 1. Bathymetry map of the Wharton and Indian Ocean Basins. Orange stars indicate the epicenters of Mw 8.6 (2.24°N 93.01°E) and Mw 8.2 (0.80°N 92.46°E) earthquakes occurred on 11 April 2012. The fault mechanisms of both the events are also shown. The triangle shows the locations of GPS stations while the pentagon shows the locations of seismometers used in the study. Ionospheric Piercing Point tracks of GPS satellites with various Pseudo Random Numbers as recorded from *umlh* GPS station during the period of doublet earthquake are shown. The onset of both the earthquakes are marked with disks along the track (relatively larger disk corresponds to Mw 8.6 earthquake). The figure maps are generated using Generic Mapping Tools (Wessel et al., 2019).

3. Methodology

3.1. GPS Derived TEC

The GPS is well established space based technique to study the ground and ionospheric variations during transient events of earthquakes. The GPS constellation consists of ~32 satellites orbiting at ~20,200 km of altitudes in equally spaced six near circular orbits. Each satellite transmits multi-frequency signals in L-band. These signals when travel from a satellite to ground receiver, they experience delay in their propagation due to the presence of ionospheric electron density along the line of sight (LOS). The observed delay is assumed to be proportional to the total number of electron density that is, TEC along the LOS from satellite to receiver. In practice, the TEC is derived from the carrier frequency signals at 1.5754 GHz (L1) and 1.2275 GHz (L2).

We extract carrier phase and pseudorange measurements from GPS Receiver Independent Exchange (RINEX) file and calculate slant TEC (sTEC) using the following equations,

$$TEC_P = 9.52 \times (P_2 - P_1) \text{ TECU}$$

$$TEC_\phi = 9.52 \times (\phi_1 - \phi_2) \text{ TECU}$$

Here, 1 TECU = 10^{16} electrons/m². P₁-pseudorange at L1 and P₂-pseudorange at L2. ϕ_1 -carrier phase at L1 and ϕ_2 -carrier phase at L2.

The estimated TEC_p remains unambiguous but noisy thus further smoothed using precise but ambiguous TEC_φ. The finally obtained TEC is the slant TEC (sTEC). It has to be noted that sTEC estimation is performed without any bias corrections. Since our interest is mainly focused on sTEC variations and not on the absolute TEC amplitudes, this practice can be afforded. GPS observations recorded at every 30s, with elevation above ~20°, are used to estimate the sTEC.

3.2. Preparation of Vertical Component Seismogram

We obtain the real seismic datasets from the IRIS database. The pre-processing of seismic observation is done using the Seismic Analysis Code (Goldstein et al., 2003). The steps are removing mean, trend, taper, filtering, instrument response filling header of source from global centroid moment tensor database (Dziewonski & Anderson, 1981) and station information.

3.3. Spectral Analysis

The estimated sTEC is further processed for frequency spectral analysis. The sTEC is filtered using a low pass moving average filter of ~9.5 mHz frequency to derive the desired signals from the sTEC, following Sunil et al., 2015. The obtained filtered TEC is denoted as dTEC. The wavelet analysis is then performed to delineate the power distribution at the resonant ionospheric signatures in dTEC. The power spectral density is estimated on a log scale.

The vertical ground motions as extracted from the seismometer observations are filtered using the second order finite impulse response Butterworth filter in frequency range of ~3 to ~7 mHz. The filtered vertical ground motion is denoted as FVGM.

3.4. Geomagnetic Field - Acoustic Wave Coupling Factor for Rayleigh Surface Waves

The manifestations of CIP at ionospheric altitudes highly depend on the alignment of vertically propagating seismic induced acoustic waves to that of the ambient geomagnetic field. In the present study, the coupling between the Rayleigh wave induced acoustic waves and ambient geomagnetic field at ionospheric altitudes is estimated using the formula (Rolland, Lognonné, & Munekane, 2011)

$$CF = k \cdot I_b$$

where k is the atmospheric wave vector and I_b is the ambient geomagnetic field vector. The launch angle of acoustic wave vector (from zenith) is calculated as

$$\theta = \tan^{-1} \left(\frac{V_A}{V_R} \right)$$

V_A is the acoustic velocity close to the ground and V_R is the Rayleigh surface wave velocity. In the present study, using $V_A \sim 348$ m/s and $V_R \sim 3,000$ m/s, the derived θ value at ground is ~6°. The coupling factor is estimated at ~350 km of ionospheric altitude. The geomagnetic field vectors are derived from International Geomagnetic Reference Field-12 model (Thébault et al., 2015).

3.5. Satellite Geometry Effect

We compute the satellite geometry effects for the ionospheric perturbations generated by the Rayleigh wave induced acoustic waves. The atmospheric propagation of seismic induced acoustic waves is largely affected by the varying satellite line of site (LOS) geometry. The varying LOS geometry leads to integration of phases of vertically propagating waves when the line of sight is normal to the incident wavefronts. Bagiya et al., (2017, 2019) proposed a simple formula, based on the Georges and Hooke (Georges & Hooke, 1970), for computing the wave phase cancellation effects during varying GPS satellite geometry for the acoustic waves emanating from

the epicenter. We use this formula to estimate the observation geometry effects for the Rayleigh wave induced acoustic waves. The formula is as follows:

$$\text{SGF}(\lambda, \varphi, h) = \exp\left(-\frac{\mathbf{k}(\lambda, \varphi, h) \cdot \mathbf{r}(\lambda, \varphi, h)}{\cos \chi}\right)$$

λ , φ , and h are the geographic longitude, geographic latitude and terrestrial altitude respectively. Absolute values of $\mathbf{k}(\lambda, \varphi, h) \cdot \mathbf{r}(\lambda, \varphi, h)$ are considered here thus the factor values vary from 0 to 1.

3.6. Background Electron Density

The background density variations are obtained in terms of TEC changes as estimated in International GNSS Service (IGS) TEC maps. By using global IGS TEC observations, the IGS iono working group computes these maps at every 15 min, 1 hr, and 2 hr (Feltens & Schaer, 1998; Wienia, 2008) (<http://cdaweb.gsfc.nasa.gov/>). Each map contains the vertical TEC estimated at latitude \times longitude grid of $2.5^\circ \times 5.0^\circ$ and IPP height of 400 km. The TEC values for the preferred geographical grid surrounding the Mw 8.6 and Mw 8.2 epicenters were extracted during the 15 min of respective earthquake occurrence time and interpolated it to obtain the variations at finer grid points.

4. Results

The GPS satellites with Pseudo Random Number (PRN) 32, 16, 19, 20, 03 and 06 were rightly orbiting over the Sumatra region during the occurrence of Sumatra 2012 doublet earthquake. The tracks of these PRNs between 08:00 and 13:00 UT from *umlh* GPS station are estimated at Ionospheric Piercing Point (IPP) altitude of ~ 350 km and shown in Figure 1 for visualizing each PRN's position during the doublet event. The IPP altitude of ~ 350 km is based on the F-region peak altitude derived from the International Reference Ionosphere-2016 model for the event day and approximate time (Bilitza et al., 2017).

The temporal evolution of seismic induced ionospheric perturbations as observed by PRN 32 and PRN 16 are presented in Figure 2 (a and b respectively). The perturbations are shown using the filtered TEC (dTEC). The time series are shown as per the IPP locations in the north and south of both the epicenters at the onset time of first CIP. Both the epicenters were separated by a small distance of ~ 182 km thus the azimuthal geometry of the stations remain same during both earthquakes. The onsets of both earthquakes are indicated by vertical lines. Corresponding to PRN 32, station *umlh* recorded a classic CIP ~ 12 min after the occurrence of the first earthquake (Figure 2a). This CIP as observed by PRN 32 from *umlh* is followed by ionospheric perturbations/oscillations which continued for ~ 66 min ($\sim 09:17$ to $\sim 10:24$ UT). The power spectrum for these oscillations is shown separately along with dTEC time series (Figure 2c). It can be noticed that these oscillations are observed preferably in the frequency range ~ 3.7 to ~ 4.4 mHz and centered on ~ 4.0 mHz. In power spectrum, the significant power of these resonant ionospheric signatures could be noticed till 10:00 UT however in time series the perturbations are still visible till $\sim 10:24$ UT. A significant CIP following the second earthquake appeared in PRN 32 observation from *umlh*. However, the second earthquake did not yield ionospheric oscillations similar to those observed during the first earthquake, especially like those with prolonged duration.

The CIP as observed by PRN 32 from other GPS stations could be noticed in Figure 2a. At station *lew*, considerable CIP are recorded after the first earthquake. Moreover, the induced ionospheric oscillations were again centered on ~ 4 mHz, though similar to those recorded at *umlh*, occurred for a smaller duration (~ 20 min). Since the amplitude of these perturbations was rather small compared to the main CIP, it cannot be identified in the power spectrum analysis of *lew* dTEC time series, thus not shown here. As for the second earthquake, PRN 32 could observe distinguishable CIP from *lew* station but could not capture any resonant ionospheric signatures during later times. Noticeable CIP could be detected by PRN 32 after both the earthquakes from *bsim* GPS station however the ionospheric oscillations similar to the *umlh* and *lew* were not observed from *bsim*. It is also important to note that the CIP amplitudes from *lew* and *bsim* remained small compared to *umlh*. The time series recorded by PRN 32 from *pbri* exhibited relatively weak CIP after both the events. Importantly, PRN 32 recorded continuous ionospheric oscillations at station *pbri* after the second earthquake. The analysis in the present study suggests that the duration of these oscillations was ~ 30 min ($\sim 11:18$ to $11:48$ UT). The power spectrum for the oscillations depicts dominant power over the frequency range of ~ 3.7 to ~ 4.4 mHz. However, such oscillations

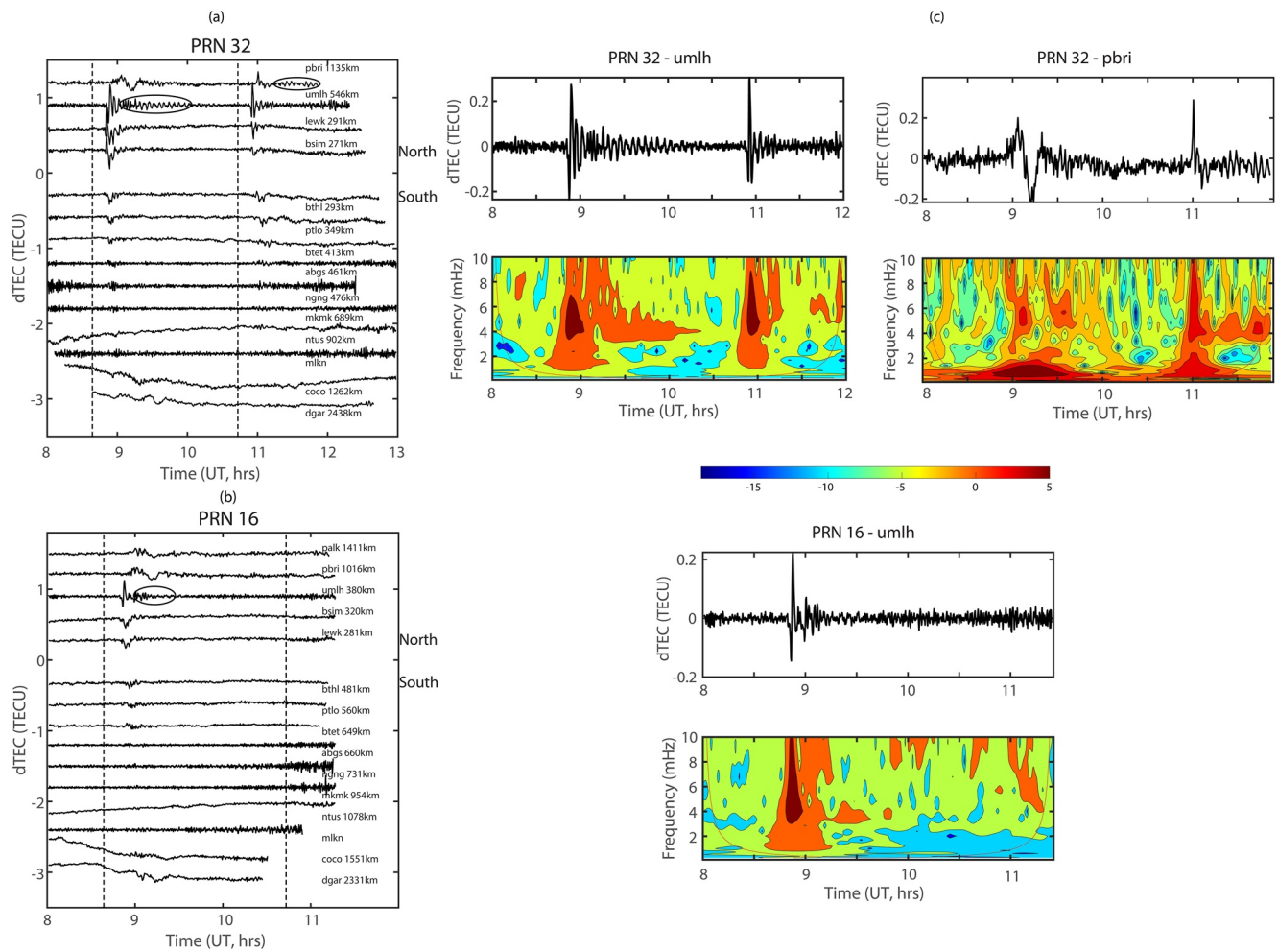


Figure 2. Temporal evolution of seismic induced ionospheric signatures as observed by (a) Pseudo Random Number (PRN) 32 and (b) PRN 16 from GPS stations of Figure 1. The resonant ionospheric signatures are highlighted in oval. Time series are categorized in the north and south based on the IPP location at the onset time of CIP during the Mw 8.6 event. The respective IPP distance from the ionospheric projection of Mw 8.6 epicenter is also shown. The vertical lines show the onset time of each event. The Mw 8.6 event occurred at 08:38:37 UT and the Mw 8.2 event at 10:43:10 UT. (c) Power spectral analysis of PRN 32 dTEC time series from *umlh* and *pbri* and of PRN 16 dTEC time series from *umlh*. The red curve shows the cone of influence. The power is shown on a logarithmic scale.

were conspicuously absent after the first earthquake in PRN 32 observations from *pbri*. From Figure 2a, it is evident that CIP evolved with higher amplitudes in the north of the epicenter. While in the south, the CIP were rather feeble and they started to disappear with increasing distance from the epicenters. The prolonged resonant ionospheric signatures could not be clearly observed in the south.

Figure 2b shows a similar analysis for PRN 16. Significant CIP and clearer ionospheric oscillations were recorded from *umlh* after the first earthquake. The dTEC time series and corresponding power spectrum for PRN 16 could be verified in Figure 2c. It should be noted that ionospheric oscillations were less intense and their duration as estimated from dTEC time series (~26 min) was relatively smaller compared to the observation of PRN 32 from *umlh*. The CIP were relatively weaker from other north stations (Figure 2b). Evidently, these stations did not observe any ionospheric oscillations in PRN 16. Further, in case of PRN 16 also, the stations in south recorded either no CIP or very weak CIP compared to the north.

So, PRN 32 and 16 recorded continuous ionospheric oscillations centered ~4 mHz after both the earthquakes over the restricted region towards NNE of the epicenters. The large amplitudes of CIP as well as oscillations are evident NNE of the epicenters (Figures 3a and 3b respectively). The tracks of PRN 32 from *umlh*, *lew* and *pbri*, PRN 16 from *umlh*, and PRN 19 from *pbri*, Figure 3c(inset), depict the spatial extent of resonant ionospheric signatures. The time series of PRN 19 from *pbri* and other stations are included in Figure S1 in Supporting

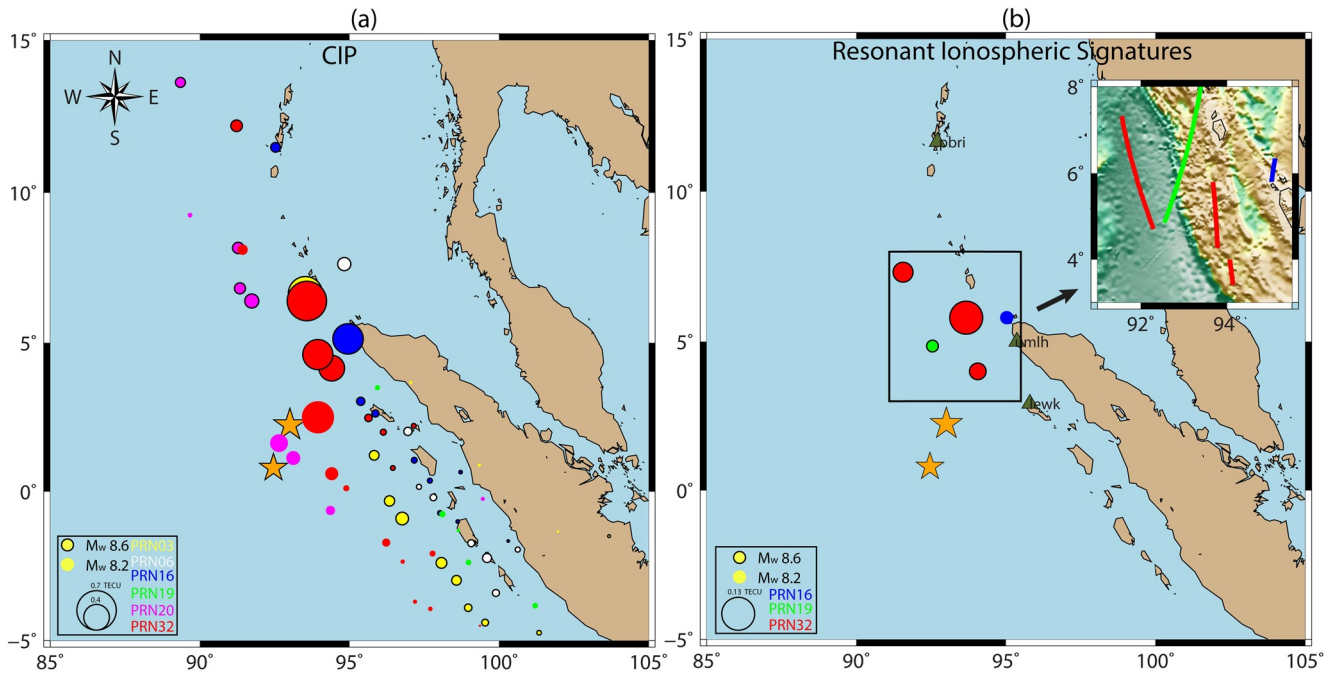


Figure 3. (a) Spatial distribution of CIP amplitude as observed by Pseudo Random Numbers (PRNs) 32, 16, 19, 20, 03 and 06 from GPS stations of Figure 1. Disk color distinguishes different PRNs and size represents the CIP amplitudes. CIP as triggered by Mw 8.6 event are outlined in black. The disks are drawn at IPP altitude of 350 km. The CIP amplitudes are multiplied by 1.5 for clear visualization. (b) Amplitude distribution of the resonant ionospheric signatures. The amplitude of resonant signatures is multiplied with 7 for clear visualization. Other details are same as of (a). (c) Spatial extent of resonant signatures along with the IPP track of respective PRN. The figure maps are generated using Generic Mapping Tools (Wessel et al., 2019).

Information S1 along with the observations of PRN 20, 03 and 06. The restricted spatial evolution of resonant ionospheric signatures is conspicuously evident during both events.

We attempt to trace the origin of these resonant signatures in the context of non-tectonic and tectonic forcing causatives. In this line, first we estimate the non-tectonic forcing mechanisms around the epicenter of Mw 8.6 event and present it in Figures 4a–4c. These mechanisms are the geomagnetic field coupling factor, observation geometry and background ionospheric electron density gradients. The effects of observation geometry have been computed by Bagiya et al. (2017, 2019) for the acoustic waves directly emanating from the epicenters. In the present study, we move a step forward and compute these effects for the wave perturbations produced by the propagating Rayleigh waves.

4.1. Geomagnetic Field Coupling Factor

Consequent to the arrival of the tectonically induced atmospheric wave perturbations at ionospheric altitudes, the non-tectonic forcing arising from the geomagnetic field - acoustic wave coupling controls the evolution of subsequent ionospheric perturbations (Bagiya et al., 2017, 2018; Heki & Ping, 2005; Rolland et al., 2013; Sunil et al., 2017). The evolution of fast propagating waves in the ionosphere after the earthquake is a complex process (Chen et al., 2011). Rolland, Lognonné, and Munekane (2011) estimated the geomagnetic field coupling factor at ionosphere altitudes for Rayleigh surface wave induced perturbations. Adopting a similar approach, we computed this factor for Rayleigh surface wave induced acoustic waves for the region of interest from the Mw 8.6 earthquake epicenter and present in Figure 4a. It could be noticed that north of the epicenter (till $\sim 10^\circ\text{N}$), the coupling between the geomagnetic field and seismic induced acoustic waves facilitate the evolution of the ionospheric perturbations. Further, non-tectonic forcing mechanism of geomagnetic field-acoustic wave coupling opposes the growth of the perturbations south of the epicenter. The coupling factor manifested in similar way during the Mw 8.2 event also (Figure S3 in Supporting Information S1). It should be noted that the resonant ionospheric signatures were absent in the further north (beyond 10°N), further south, and east of the epicenters even though these directions are considered as favorable from the point of geomagnetic field-acoustic wave coupling.

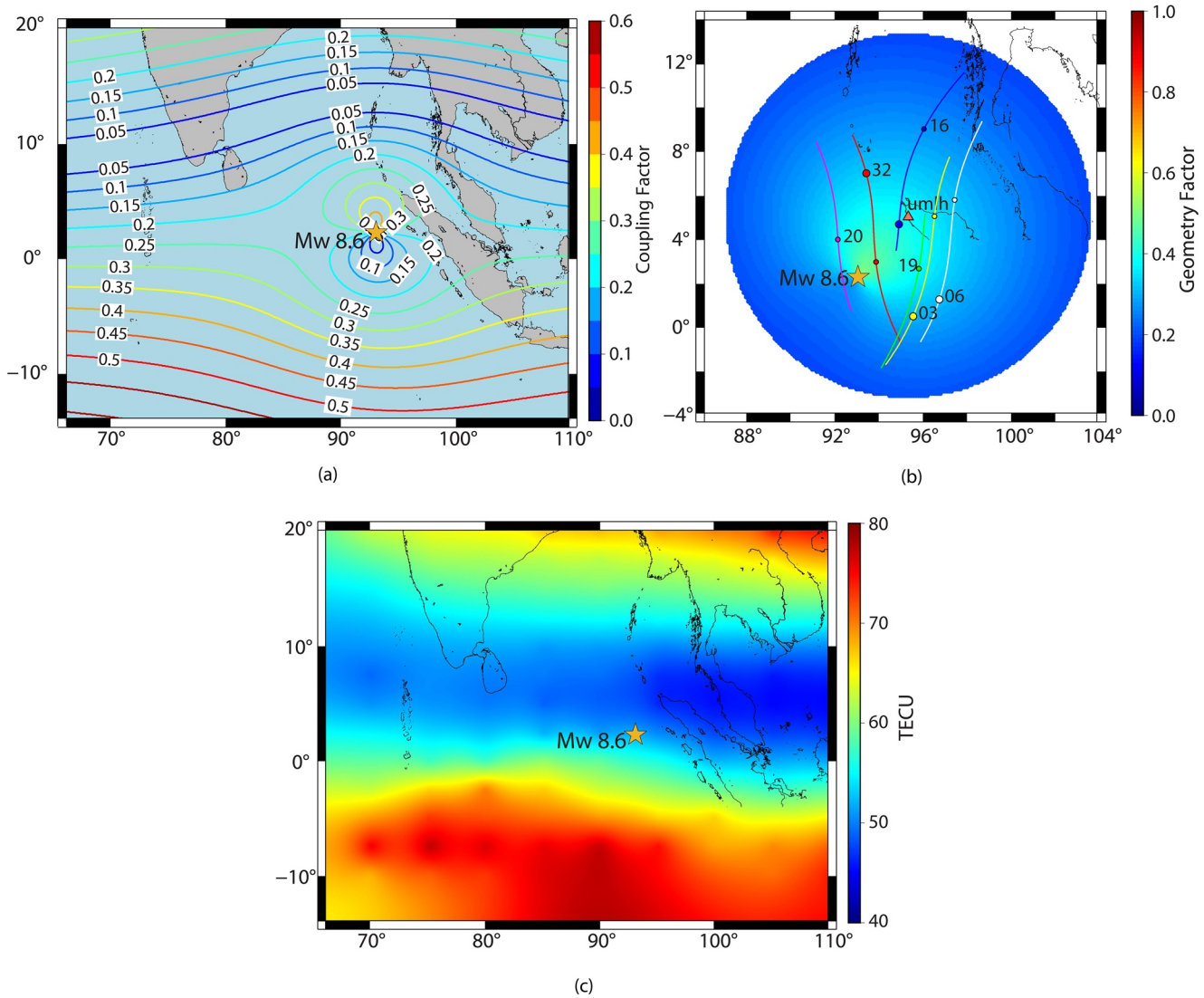


Figure 4. Manifestations of non-tectonic forcing mechanisms during the Mw 8.6 event. (a) Geomagnetic field acoustic wave coupling factor by considering the Rayleigh wave as seismic source (b) satellite geometry factor for the Rayleigh wave induced acoustic waves. The factor is computed for the GPS station of *umlh*. IPP tracks of Pseudo Random Numbers visible during the time period of 8–13 UT are also shown. Factors of (a) and (b) are computed at altitude of 350 km (c) ambient ionospheric electron density gradient. The figure maps are generated using Generic Mapping Tools (Wessel et al., 2019).

4.2. Satellite Geometry

In order to study the GPS satellite geometry effects, we compute the satellite geometry factor for the Rayleigh wave induced acoustic wave perturbations in the atmosphere following the approach proposed by Bagiya et al. (2017, 2019). Figure 4b shows the estimated geometry factor for the GPS station of *umlh* during the Mw 8.6 event. The geometry factor for other selected stations of *bthl*, *btet*, *pbri*, *coco* and *dgar* are presented in Figure S2 in Supporting Information S1. For GPS observation geometry, Rolland et al. (2011a) reported that low elevation satellite geometries (≤ 40) are more suitable to detect the Rayleigh wave induced ionospheric perturbations. The estimated satellite geometry factor in this study corroborates this well. It is pertinent to note that the elevations for PRN 32 from *umlh* was $\sim 60^\circ$ while recording the resonant ionospheric signatures. This could be verified with the moderate geometry factor values along the track of PRN 32 in Figure 4b. Yet PRN 32 recorded significant amplitude of CIP as well as resonant signatures from *umlh* station.

From *pbri* GPS station PRN 32 could not record any noticeable resonant signatures after the Mw 8.6 event though geometry was moderately favorable. It should be noted that geomagnetic coupling was not so favorable over this

region. Further, PRN 32 recorded considerable resonant signatures after the Mw 8.2 event where geomagnetic field coupling factor and satellite geometry both were quite favorable. We believe that observation geometry effects after the Mw 8.2 event can be easily visualized based on the estimation performed after the Mw 8.6 event (Figures 4b and S2 in Supporting Information S1) and thus we do not repeat the calculation of observation geometry factor for the second event.

Based on Figures 4b and S2 in Supporting Information S1, we show that GPS satellite geometry were quite favorable from the stations located in the south. Also, the geomagnetic coupling factor was favorable in further south, but distinguishable CIP with low amplitudes could only be recorded at a few of the stations (Figure 2). No clear resonant ionospheric signatures were evident in the south.

4.3. Background Electron Density

The ambient ionospheric density plays a vital role in manifesting the amplitude of any ionospheric perturbations (Bagiya et al., 2019). In case of higher background electron density, the perturbations can grow with higher amplitudes and vice versa. We obtain the electron density variations at altitude of 400 km using the IGS TEC maps and present in Figures 4b and S3 in Supporting Information S1. It could be noted that higher density manifests south of the epicenters while in the north the density remained relatively less. It has to be noted that IPP altitude in the present study is considered at 350 km. The electron density measurements at specific ionospheric altitudes are not available. Thus, the obtained TEC variations are considered to show the variation of ionization density at other altitudes as well (Bagiya et al., 2019).

To study the contributions of tectonic forcing in generating the resonant ionospheric signatures, we looked into the manifestations of long-period Rayleigh waves during these events. The propagation of long period Rayleigh waves in the ionosphere is displayed in the hodochrone (Figure S4 in Supporting Information S1) estimating the velocity ~ 2.65 km/s.

4.4. Rayleigh Surface Wave Radiation Pattern

The propagation characteristics of seismic surface waves largely depend on the source attributes in addition to the local geological structures. The source attributes were not so simple during the Sumatra 2012 doublet event. The bilateral rupture in the WNW-ESE direction triggered the Mw 8.6 event and then bilateral rupture was activated in NNE to SSW direction which was followed by westward rupture and at last rupture propagated in west of the epicenter (Yue et al., 2012). Duputel et al., (2012) further analyzed the long period surface wave amplitudes to derive the rupture directivity during this doublet event. Based on the surface wave radiation pattern they derived, significantly higher portion of the seismic energy during the Mw 8.6 event propagated westward. The Rayleigh surface wave radiation pattern during the Mw 8.6 event is referred from Figure 6c of Duputel et al., 2012.

We analyze the vertical ground motions from the seismometers located in the vicinity of the epicenters and present in Figure 5. Since the atmosphere is mostly sensitive to vertical ground motion, we extract the corresponding response from seismometers. All seismic stations have a corner frequency at 120s except PBA which reaches 240s. To clearly distinguish the onset of low frequency we filtered the data set with a bandpass filter of ~ 3 to ~ 7 mHz. The seismic response from CHTO observed low amplitude compared to other stations as less portion of the total energy was directed in the NNE direction which corroborates with the directivity of seismic energy propagation highlighted by Duputel et al., 2012. As we can see in Figure 5 the wave amplitudes at PBA and PSI were high which could be attributed to its relatively lesser distance from the epicenter.

Duputel et al., (2012) further highlight that the Mw 8.6 earthquake source complexity causes Rayleigh surface waves of relatively higher energy at ~ 250 s (~ 4 mHz). This excess of low-frequency energy is explained by a two-point source model. We propose this could make the Mw 8.6 Sumatra 2012 earthquake particularly efficient to excite the 4 mHz resonance in the atmosphere. Note that the Mw 8.2 earthquake, well modeled with a single point source, does not show this feature. This could indicate that the long-lasting resonant oscillations observed after the Mw 8.2 earthquake event are also excited by the R2 wavetrain (first Rayleigh Wave train travel along major arc) of the Mw 8.6 event. The R2 wave train indeed happens to arrive immediately following the Mw 8.2 earthquake that occurred 2 hr after the Mw 8.6 event.

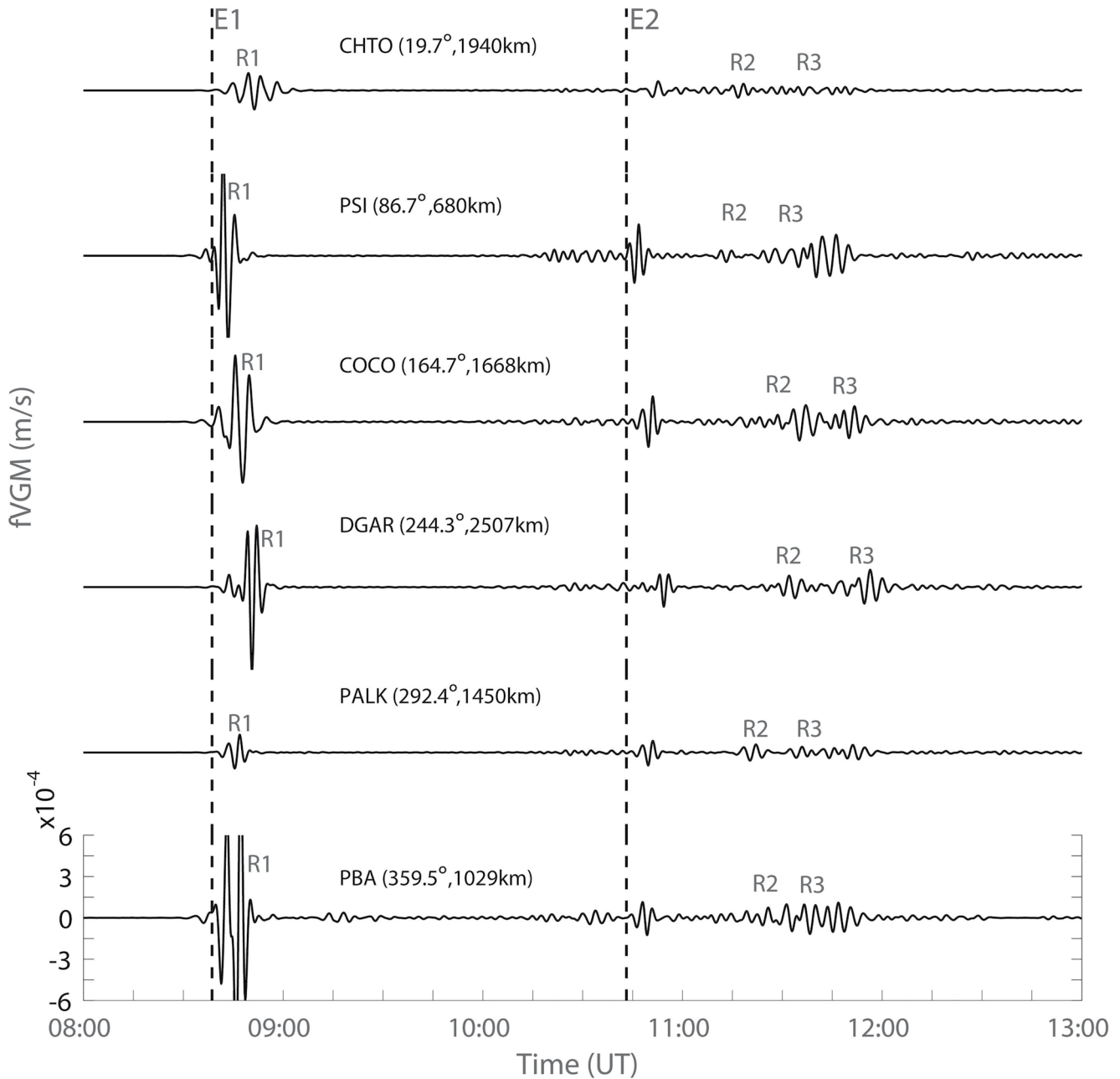


Figure 5. Filtered (3–7 mHz) vertical ground motions (fVGM) at seismometer stations of Figure 1. Azimuth and great-circle distance of each station with respect to the Mw 8.6 source are shown. Origin time of both events with R1 (first Rayleigh Wave train travel along minor arc), R2 (first Rayleigh Wave train travel along major arc) and R3 (second Rayleigh Wave train travel along minor arc after one round) surface waves for first event are marked.

4.5. R2 Surface Wavetrain After the Mw 8.6 Earthquake

The Mw 8.6 doublet earthquake was a major strike-slip event trending in the WNW–ESE direction (Singh et al., 2017; Yue et al., 2012), and the subsequent one shares similar faulting characteristics. From Figure 5, both the earthquakes did generate discernible vertical ground motion at the frequencies of interest. However, a more intense vertical response is associated with the later Mw 8.2 event. We attribute this more intense vertical response to a possible recording of R2 and R3 waves (second Rayleigh Wave train travel along minor arc) generated by the first event which arrived during the time window of the second earthquake. It is needless to mention that the R2 and R3 waves can also induce the Earth's free oscillations at its fundamental modes which is evident by the presence of prominent signals at frequencies in the range ~ 3.7 to ~ 4.4 mHz in Figure 5. The ionospheric

oscillations observed after Mw 8.2 event by PRN 32 from *pbri* GPS station might contain a major contribution from the Earth's free oscillations triggered by the Mw 8.6 event at these resonant frequencies.

5. Discussion

During any earthquake the solid earth transfers $\sim 10^{-4}$ to $\sim 10^{-5}$ of the seismic energy to the adjacent atmosphere through solid Earth-atmosphere coupling (Lognonné et al., 2006; Watada & Kanamori, 2010). The transfer of this seismic energy is maximum at the frequencies where the Earth and atmosphere have resonance. As mentioned, the spheroidal modes of the Earth's background free oscillations (a) ${}_0S_{29}$ (~ 3.7 mHz) and (b) ${}_0S_{37}$ (~ 4.4 mHz) overlap with the atmospheric acoustic modes and trigger the resonance between the Earth and the atmosphere. Thus, the effects due to seismic energy centered on these frequencies manifest best in the atmosphere. It is pertinent to note that the observed prolonged ionospheric oscillations are preferably associated with frequencies in the range ~ 3.7 to ~ 4.4 mHz.

From tectonic point of view, the Mw 8.6 earthquake source triggered Rayleigh surface waves at ~ 4 mHz with comparatively higher energy (Duputel et al., 2012). It is assumed that this excess energy played an important role in generating the observed resonant ionospheric signatures after the Mw 8.6 event. It is pertinent to note that the surface waves generated during the Mw 8.6 earthquake triggered the Earth's free oscillations $\sim 2:30$ hr after the occurrence of the event (Duputel et al., 2012). Hence, origin of the prolonged ionospheric oscillations which were recorded immediately after the classic CIP arrival (after ~ 10 min) during the Mw 8.6 event cannot be traced to the Earth's free oscillations and its subsequent resonance with the atmosphere at fundamental acoustic modes. However, the resonance ionospheric signatures observed after the Mw 8.2 earthquake has a close association with R2 wave train arriving after the Mw 8.6 event.

Further, evolution of the resonant signatures as well as of CIP are subjected to the non-tectonic forcing mechanisms that prevail at ionospheric altitudes (e.g., Bagiya et al., 2019; Rolland et al., 2013). Significant amplitudes of CIP and resonant signatures in the NNE of the epicenters are supported by the favorable geomagnetic field coupling factor and satellite geometry factor. However, in the further north ($\sim 10^\circ\text{N}$ and above), further south ($\sim 2^\circ\text{S}$ and below), and west of the epicenters the signatures could not be seen despite the supportive coupling factor and observation geometry. This possibly hints that more robust methodology is desired to decode the effects of non-tectonic factors from the dominant seismic forcing. According to Chen et al., (2011), initial ionospheric perturbations may not propagate fully along the geomagnetic field lines and thus the effects of geomagnetic field could not be derived conclusively for initial perturbations. Further, earthquakes occurring at various latitudes can lead to generation of ionospheric perturbations of similar magnitudes. This aspect needs to be scrutinized in terms of limited applicability of geomagnetic field factor. More studies are underway in this line.

6. Conclusion

The ionospheric oscillations recorded for prolonged duration during the 11 April 2012 Sumatra doublet earthquake are explained in terms of acoustic resonant coupling between the terrestrial surface and its atmosphere. The north-south amplitude anisotropy of resonant ionospheric signatures following the doublet event are discussed by invoking the manifestations of seismic forcing around the epicenter in addition to the non-tectonic forcing mechanisms of geomagnetic field coupling factor and observation geometry. The prominent generation of seismic surface waves at ~ 4 mHz (Duputel et al., 2012) and the R2 surface wave train after the Mw 8.6 event assisted in explaining the resonance observed in the GPS-TEC after the Mw 8.6 and Mw 8.2 event respectively. The association of resonant ionospheric signatures recorded following the Mw 8.2 event to the R2 Rayleigh surface wave train of the Mw 8.6 event is a rather novel proposition and depicts the atmospheric response to the terrestrial free oscillations at acoustic modes. It is suggested that resonant ionospheric signatures may contain information on the rupture process of large and complex earthquakes.

Data Availability Statement

The International GNSS Service (IGS) and SOPAC are duly acknowledged for the IGS GPS data. GPS data are downloaded from <http://sopac-csrc.ucsd.edu/>. The Incorporated Research Institutions for Seismology data management center (IRIS-DMC) is duly acknowledged for the seismometer data. Seismometer data are downloaded from <http://ds.iris.edu/ds/>.

Acknowledgments

We sincerely thank Lucie Rolland and Anthony Sladen, Université Côte d'Azur, Géoazur, S. P. Anand, Indian Institute of Geomagnetism and P. S. Sunil, Cochin University of Science and Technology for useful discussions. The Earth Observatory of Singapore, Indonesian Institute of Sciences (LIPI) and SOPAC are duly acknowledged for the Sumatran GPS Array network data. S. Nayak thank the Department of Science and Technology (DST), Government of India for providing research fellowship. This work is part of the interdisciplinary program Coupled Lithosphere-Atmosphere-Ionosphere-Magnetosphere System (CLAIMS) of Indian Institute of Geomagnetism and supported by DST, India.

References

- Artru, J., Farges, T., & Lognonné, P. (2004). Acoustic waves generated from seismic surface waves: Propagation properties determined from Doppler sounding observations and normal-mode modelling. *Geophysical Journal International*, *158*(3), 1067–1077. <https://doi.org/10.1111/j.1365-246X.2004.02377.x>
- Astafeyeva, E., & Heki, K. (2009). Dependence of waveform of near-field coseismic ionospheric disturbances on focal mechanisms. *Earth Planets and Space*, *61*, 939–943. <https://doi.org/10.1186/bf03353206>
- Astafeyeva, E., Lognonné, P., & Rolland, L. (2011). First ionospheric images of the seismic fault slip on the example of the Tohoku-oki earthquake. *Geophysical Research Letters*, *38*(22), L22104. <https://doi.org/10.1029/2011GL049623>
- Astafeyeva, E., Rolland, L. M., & Sladen, A. (2014). Strike-slip earthquakes can also be detected in the ionosphere. *Earth and Planetary Science Letters*, *405*, 180–193. <https://doi.org/10.1016/j.epsl.2014.08.024>
- Bagiya, M. S., Sunil, A. S., Rolland, L., Nayak, S., Ponraj, M., Thomas, D., & Ramesh, D. S. (2019). Mapping the impact of non-tectonic forcing mechanisms on GNSS measured coseismic ionospheric perturbations. *Scientific Reports*, *9*(1), 1–15. <https://doi.org/10.1038/s41598-019-54354-0>
- Bagiya, M. S., Sunil, A. S., Sunil, P. S., Sreejith, K. M., Rolland, L., & Ramesh, D. S. (2017). Efficiency of coseismic ionospheric perturbations in identifying crustal deformation pattern: Case study based on Mw 7.3 May Nepal 2015 earthquake. *Journal of Geophysical Research: Space Physics*, *122*(6), 6849–6857. <https://doi.org/10.1002/2017JA024050>
- Bagiya, M. S., Sunil, P. S., Sunil, A. S., & Ramesh, D. S. (2018). Coseismic contortion and coupled nocturnal ionospheric perturbations during 2016 Kaikoura, Mw 7.8 New Zealand earthquake. *Journal of Geophysical Research: Space Physics*, *123*(2), 1477–1487. <https://doi.org/10.1002/2017JA024584>
- Bilitza, D., Altadill, D., Truhlik, V., Shubin, V., Galkin, I., Reinisch, B., & Huang, X. (2017). International reference ionosphere 2016: From ionospheric climate to real-time weather predictions. *Space Weather*, *15*(2), 418–429. <https://doi.org/10.1002/2016SW001593>
- Cahyadi, M. N., & Heki, K. (2013). Ionospheric disturbances of the 2007 Bengkulu and the 2005 Nias earthquakes, Sumatra, observed with a regional GPS network. *Journal of Geophysical Research: Space Physics*, *118*(4), 1777–1787. <https://doi.org/10.1002/jgra.50208>
- Cahyadi, M. N., & Heki, K. (2015). Coseismic ionospheric disturbance of the large strike-slip earthquakes in North Sumatra in 2012: Mw dependence of the disturbance amplitudes. *Geophysical Journal International*, *200*(1), 116–129. <https://doi.org/10.1093/gji/ggu343>
- Calais, E., & Bernard, J. (1995). GPS detection of ionospheric perturbations following the January 17, 1994. *Northridge earthquake*, *22*(9), 1045–1048. <https://doi.org/10.1029/95gl00168>
- Chen, C. H., Saito, A., Lin, C. H., Liu, J. Y., Tsai, H. F., Tsubawa, T., et al. (2011). Long-distance propagation of ionospheric disturbance generated by the 2011 off the Pacific coast of Tohoku Earthquake. *Earth Planets and Space*, *63*(7), 881–884. <https://doi.org/10.5047/eps.2011.06.026>
- Choosakul, N., Saito, A., Iyemori, T., & Hashizume, M. (2009). Excitation of 4-min periodic ionospheric variations following the great Sumatra-Andaman earthquake in 2004. *Journal of Geophysical Research: Space Physics*, *114*, A10313. <https://doi.org/10.1029/2008JA013915>
- Chum, J., Hruska, F., Zednik, J., & Lastovicka, J. (2012). Ionospheric disturbances (infrasound waves) over the Czech Republic excited by the 2011 Tohoku earthquake. *Journal of Geophysical Research: Space Physics*, *117*(A8), A08319. <https://doi.org/10.1029/2012JA017767>
- Chum, J., Liu, J. Y., Podolská, K., & Šindelářová, T. (2017). Infrasound in the ionosphere from earthquakes and typhoons. *Journal of Atmospheric and Solar-Terrestrial Physics*, *171*(May), 72–82. <https://doi.org/10.1016/j.jastp.2017.07.022>
- Chum, J., & Podolská, K. (2018). 3D analysis of GW propagation in the ionosphere. *Geophysical Research Letters*, *45*(21), 11562–11571. <https://doi.org/10.1029/2018GL079695>
- Ducic, V., Artru, J., & Lognonné, P. (2003). Ionospheric remote sensing of the Denali Earthquake Rayleigh surface waves. *Geophysical Research Letters*, *30*(18), 1951. <https://doi.org/10.1029/2003GL017812>
- Duputel, Z., Kanamori, H., Tsai, V. C., Rivera, L., Meng, L., Ampuero, J.-P., & Stock, J. M. (2012). The 2012 Sumatra great earthquake sequence. *Earth and Planetary Science Letters*, *351*–352, 247–257. <https://doi.org/10.1016/j.epsl.2012.07.017>
- Dziewonski, A. M., & Anderson, D. L. (1981). Preliminary reference Earth model. *Physics of the Earth and Planetary Interiors*, *25*(4), 297–356. [https://doi.org/10.1016/0031-9201\(81\)90046-7](https://doi.org/10.1016/0031-9201(81)90046-7)
- Feltens, J., & Schaer, S. (1998). *IGS position paper: IGS Analysis Centers Workshop ESOC*. February 9–11, 1998, 1–7.
- Fukao, Y., Nishida, K., Suda, N., Nawa, K., & Kobayashi, N. (2002). A theory of the Earth's background free oscillations. *Journal of Geophysical Research: Solid Earth*, *107*(B9), ESE 11-1–ESS 11-10. <https://doi.org/10.1029/2001JB000153>
- Garcia, R., Crespon, F., Ducic, V., & Lognonné, P. (2005). Three-dimensional ionospheric tomography of post-seismic perturbations produced by the Denali earthquake from GPS data. *Geophysical Journal International*, *163*(3), 1049–1064. <https://doi.org/10.1111/j.1365-246X.2005.02775.x>
- Georges, T. M., & Hooke, W. H. (1970). Wave-induced fluctuations in ionospheric electron content: A model indicating some observational biases. *Journal of Geophysical Research*, *75*, 6295–6308. <https://doi.org/10.1029/ja075i031p06295>
- Gilbert, F., & Macdon, G. J. (1960). Free oscillations of the Earth I. *Torroidal Oscillations*, *65*(2). <https://doi.org/10.1029/jz065i002p00675>
- Goldstein, P., Dodge, D., Firpo, M., & Minner, L. (2003). 85.5 SAC2000: Signal processing and analysis tools for seismologists and engineers. *International Geophysics*, *81*(PART B), 1613–1614. [https://doi.org/10.1016/S0074-6142\(03\)80284-X](https://doi.org/10.1016/S0074-6142(03)80284-X)
- Heki, K., & Ping, J. (2005). Directivity and apparent velocity of the coseismic ionospheric disturbances observed with a dense GPS array. *Earth and Planetary Science Letters*, *236*(3–4), 845–855. <https://doi.org/10.1016/j.epsl.2005.06.010>
- Jones, R. M., & Georges, T. M. (1976). Infrasound from convective storms. III. Propagation to the ionosphere. *Journal of the Acoustical Society of America*, *59*(4), 765–779. <https://doi.org/10.1121/1.380942>
- Kanamori, H., & Mori, J. (1992). Harmonic excitation of mantle Rayleigh waves by the 1991 eruption of Mount Pinatubo, Philippines. *Geophysical Research Letters*, *19*(7), 721–724. <https://doi.org/10.1029/92GL00258>
- Kobayashi, N., & Nishida, K. (1998). Continuous excitation of planetary free oscillations by atmospheric disturbances. *Nature*, *395*(6700), 357–360. <https://doi.org/10.1038/26427>

- Kovach, R. L., & Anderson, D. L. (1967). Study of the energy of the free oscillations of the Earth. *Journal of Geophysical Research (1896–1977)*, 72(8), 2155–2168. <https://doi.org/10.1029/JZ072i008p02155>
- Liu, J. Y., Chen, C. H., Lin, C. H., Tsai, H. F., Chen, C. H., & Kamogawa, M. (2011). Ionospheric disturbances triggered by the 11 March 2011 M9.0 Tohoku earthquake. *Journal of Geophysical Research: Space Physics*, 116(A6), A06319. <https://doi.org/10.1029/2011JA016761>
- Lognonne, P., Clevede, E., & Kanamori, H. (1998). Computation of seismograms and atmospheric oscillations by normal-mode summation for a spherical earth model with realistic atmosphere. *Geophysical Journal International*, 135, 388–406. <https://doi.org/10.1046/j.1365-246x.1998.00665.x>
- Lognonné, P., Garcia, R., Crespon, F., Occhipinti, G., Kherani, A., & Artru-Lambin, J. (2006). Seismic waves in the ionosphere. *Europhysics News*, 37(4), 11–15. <https://doi.org/10.1051/epn:2006401>
- Maruyama, T., & Shinagawa, H. (2014). Infrasonic sounds excited by seismic waves of the 2011 Tohoku-oki earthquake as visualized in ionograms. *Journal of Geophysical Research: Space Physics*, 119(5), 4094–4108. <https://doi.org/10.1002/2013JA019707>
- Maruyama, T., Tsugawa, T., Kato, H., Ishii, M., & Nishioka, M. (2012). Rayleigh wave signature in ionograms induced by strong earthquakes. *Journal of Geophysical Research: Space Physics*, 117(A8), A08306. <https://doi.org/10.1029/2012JA017952>
- Nawa, K., Suda, N., Fukao, Y., Sato, T., Aoyama, Y., & Shibuya, K. (1998). Incessant excitation of the Earth's free oscillations. *Earth Planets and Space*, 50(1), 3–8. <https://doi.org/10.1186/BF03352080>
- Nishida, K., Kobayashi, N., & Fukao, Y. (2000). Resonant oscillations between the solid earth and the atmosphere. *Science*, 287(5461), 2244–2246. <https://doi.org/10.1126/science.287.5461.2244>
- Reddy, C. D., Shrivastava, M. N., Seemala, G. K., González, G., & Baez, J. C. (2016). Ionospheric Plasma Response to M_w 8.3 Chile Illapel Earthquake on September 16, 2015. *Pure and Applied Geophysics*, 173, 1451–1461. <https://doi.org/10.1007/s00024-016-1282-3>
- Rolland, L. M., Lognonné, P., Astafyeva, E., Kherani, E. A., Kobayashi, N., Mann, M., & Munekane, H. (2011). The resonant response of the ionosphere imaged after the 2011 off the Pacific coast of 689 Tohoku Earthquake. *Earth Planets and Space*, 63(7), 853–857. <https://doi.org/10.5047/eps.2011.06.020>
- Rolland, L. M., Lognonné, P., & Munekane, H. (2011). Detection and modeling of Rayleigh wave induced patterns in the ionosphere. *Journal of Geophysical Research: Space Physics*, 116(A5), 1–18. <https://doi.org/10.1029/2010ja016060>
- Rolland, L. M., Vergnolle, M., Nocquet, J.-M., Sladen, A., Dessa, J.-X., Tavakoli, F., et al. (2013). Discriminating the tectonic and non-tectonic contributions in the ionospheric signature of the 2011, Mw7.1, dip-slip Van earthquake, Eastern Turkey. *Geophysical Research Letters*, 40(11), 2518–2522. <https://doi.org/10.1002/grl.50544>
- Singh, S. C., Hananto, N., Qin, Y., Leclerc, F., Avianto, P., Tapponnier, P. E., et al. (2017). The discovery of a conjugate system of faults in the Wharton Basin intraplate deformation zone. *Science Advances*, 3(1). <https://doi.org/10.1126/sciadv.1601689>
- Suda, N., Nawa, K., & Fukao, Y. (1998). Earth's background free oscillations. *Science*, 279(5359), 2089–2091. <https://doi.org/10.1126/science.279.5359.2089>
- Sunil, A. S., Bagiya, M. S., Catherine, J., Rolland, L., Sharma, N., Sunil, P. S., & Ramesh, D. S. (2017). Dependence of near field co-seismic ionospheric perturbations on surface deformations: A case study based on the April, 25 2015 Gorkha Nepal earthquake. *Advances in Space Research*, 59(5), 1200–1208. <https://doi.org/10.1016/j.asr.2016.11.041>
- Sunil, A. S., Bagiya, M. S., Reddy, C. D., Kumar, M., & Sai, D. (2015). Post-seismic ionospheric response to the 11 April 2012 East Indian Ocean doublet earthquake. *Earth Planets and Space*, 67, 37. <https://doi.org/10.1186/s40623-015-0200-8>
- Tanimoto, T., Um, J., Nishida, K., & Kobayashi, N. (1998). Earth's continuous oscillations observed on seismically quiet days. *Geophysical Research Letters*, 25(10), 1553–1556. <https://doi.org/10.1029/98GL01223>
- Thébault, E., Finlay, C. C., Beggan, C. D., Alken, P., Aubert, J., Barrois, O., et al. (2015). International geomagnetic reference field: The 12th generation international geomagnetic reference field-The twelfth generation. *Earth Planets and Space*, 67(1). <https://doi.org/10.1186/s40623-015-0228-9>
- Trabant, C., Hutko, A. R., Bahavar, M., Karstens, R., Ahern, T., & Aster, R. (2012). Data products at the IRIS DMC: Stepping stones for research and other applications. *Seismological Research Letters*, 83(5), 846–854. <https://doi.org/10.1785/0220120032>
- Tsugawa, T., Saito, A., Otsuka, Y., Nishioka, M., Maruyama, T., Kato, H., et al. (2011). Ionospheric disturbances detected by GPS total electron content observation after the 2011 off the Pacific coast of Tohoku Earthquake. *Earth Planets and Space*, 63(7), 66–879. <https://doi.org/10.5047/eps.2011.06.035>
- Watada, S. (1995). *Part I: Near-source acoustic coupling between the atmosphere and the solid earth during volcanic eruptions Part II: Nearfield normal mode amplitude anomalies of the landers earthquake*: California Institute of Technology.
- Watada, S., & Kanamori, H. (2010). Acoustic resonant oscillations between the atmosphere and the solid earth during the 1991 Mt. Pinatubo eruption. *Journal of Geophysical Research: Solid Earth*, 115(B12), B12319. <https://doi.org/10.1029/2010JB007747>
- Wessel, P., Luis, J. F., Uieda, L., Scharroo, R., Wobbe, F., Smith, W. H. F., & Tian, D. (2019). The generic mapping tools version 6. *Geochemistry, Geophysics, Geosystems*, 20(11), 5556–5564. <https://doi.org/10.1029/2019GC008515>
- Wienia, R. J. (2008). *Use of Global Ionospheric Maps for Precise Point Positioning* (Vol. 132).
- Yue, H., Lay, T., & Koper, K. D. (2012). En échelon and orthogonal fault ruptures of the 11 April 2012 great intraplate earthquakes. *Nature*, 490(7419), 245–249. <https://doi.org/10.1038/nature11492>